PHYSICAL SCIENCES

Magnetic resonance insights into the heterogeneous, fractal-like kinetics of chemically recyclable polymers

Sophia N. Fricke[1]*, Shira Haber[2], Mutian Hua[2], Mia Salgado[1], Brett A. Helms[2,3], Jeffrey A. Reimer[1,2]*

Moving toward a circular plastics economy is a vital aspect of global resource management. Chemical recycling of plastics ensures that high-value monomers can be recovered from depolymerized plastic waste, thus enabling circular manufacturing. However, to increase chemical recycling throughput in materials recovery facilities, the present understanding of polymer transport, diffusion, swelling, and heterogeneous deconstruction kinetics must be systematized to allow industrial-scale process design, spanning molecular to macroscopic regimes. To develop a framework for designing depolymerization processes, we examined acidolysis of circular polydiketoenamine elastomers. We used magnetic resonance to monitor spatially resolved observables in situ and then evaluated these data with a fractal method that treats nonlinear depolymerization kinetics. This approach delineated the roles played by network architecture and reaction medium on depolymerization outcomes, yielding parameters that facilitate comparisons between bulk processes. These streamlined methods to investigate polymer hydrolysis kinetics portend a general strategy for implementing chemical recycling on an industrial scale.

INTRODUCTION

The transition from a linear to a circular economy hinges on widespread implementation of chemically recyclable plastics with high materials efficiency and low process intensity (*1*–*3*). The development of strategies for chemical, rather than mechanical, recycling of plastics ensures that high-value monomers can be recovered from depolymerized plastic waste—ideally the original monomers, so that circular manufacturing becomes possible. Practical realization of this goal is predicated upon an ability to understand and influence the molecular mechanisms underpinning polymer circularity (*4*).

However, tracking polymer deconstruction is fraught with the difficulty of disentangling concurrent swelling, diffusion, and time-dependent reaction kinetics. To understand and control the kinetic factors that influence this heterogeneous process, it is necessary to monitor this process in situ with rigorous spatiotemporal specificity and adequately treat its nonlinearity. Nuclear magnetic resonance (NMR)—in the forms of relaxometry, spectroscopy, and imaging—has collectively emerged as a powerful and nondestructive technique to track complex processes in situ with chemical, spatial, and temporal specificity (*5*–*7*). Moreover, the information gained spans broad length and timescales, from the order of chemical bonds in the angstrom range for structure determination to macroscopic volumes on the order of cubic centimeters or more, and captures phenomena occurring in timescales from submillisecond chemical exchange and diffusion to the scope of multiday reaction processes.

Here, we examine the acid-catalyzed deconstruction of polydiketoenamines (PDKs), exemplary circular plastics whose molecular engineering enables deconstruction to constituent triketone and amine monomers in strong aqueous acid. We varied both PDK cross-linking density and the acid type and measured by using magnetic resonance (MR) techniques the reaction kinetics. Notably, we find that both the rate coefficient and reaction order are, in most cases, time dependent. Underlying this behavior, we find that polymer swelling governs the initial reaction rates and the later stages of reaction are dominated by molecular diffusion. All reaction rates decrease in time, although in a manner that is nonlinear and nonuniform with variation of the acid anion or polymer cross-linking density. We present a fractal treatment of the reaction kinetics that neatly incorporates this nonlinearity into a rate law model.

RESULTS

PDK resins can be formulated on the basis of their constituent triketone and amine monomers, similar to polyurethane and epoxy resins. The diketoenamine bond undergoes hydrolysis in strong aqueous acid as depicted in Fig. 1 (*8*–*10*). By altering the chain length of the triketone monomer unit and varying the acid anion, it is possible to control both the activation energy and the diffusive transport of the aqueous reactant that determine the hydrolysis rate, thereby enabling the recycling of mixtures of PDK variants that have different properties, without relying on sorting (*11*). Acidolysis, however, is confounded by the concurrent processes of polymer swelling, diffusion, and hydrolytic reaction, all of which are difficult to disentangle because they are interdependent and vary with time. Nonetheless, an understanding of these phenomena separately is critical for rational tuning of material properties and design of the corresponding recycling processes.

NMR is an ideal tool to examine the phenomenology shown in Fig. 1 in situ because it offers chemical and spatial specificity in a nondestructive way (*12*–*19*). The spin–spin relaxation rate ($R_2 = T_2^{-1}$) and self-diffusion coefficient (D) are NMR measurables that relate to polymer swelling behavior and phase dynamics mediated by Fickian diffusion of water, as well as the tortuous diffusion pathways of released monomers and oligomer chains in an increasingly porous polymer network. Localized changes in spin dynamics can be unambiguously mapped with imaging (*20*, *21*). We surmise that swelling and diffusion strongly influence the observed rate law

[1]Department of Chemical and Biomolecular Engineering, University of California, Berkeley, Berkeley, CA 94720, USA. [2]Materials Sciences Division, Lawrence Berkeley National Laboratory, Berkeley, CA 94720, USA. [3]The Molecular Foundry, Lawrence Berkeley National Laboratory, Berkeley, CA 94720, USA.
*Corresponding author. Email: snfricke@berkeley.edu (S.N.F.); reimer@berkeley.edu (J.A.R.)

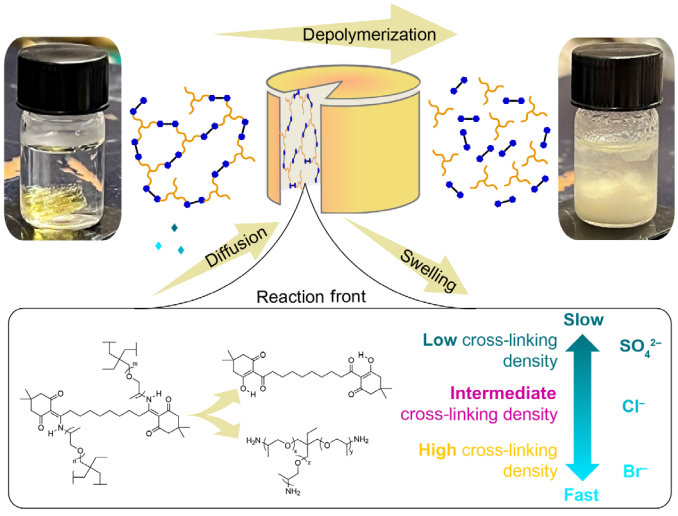

Fig. 1. A depiction of PDK acidolysis. A cross-linked PDK network is depolymerized into a triketone monomer and a tribranched amine-terminated cross-linker, as described in Methods. The reaction front is influenced by both swelling and diffusion processes, as depicted in the lower panel. The overall reaction rate is also affected by cross-linker size and the water-ordering nature of the acid anion, as shown in the lower right panel. The arrows for "Diffusion," "Swelling," and the panel "Reaction front" respectively represent transport of released monomers to solution, water into the polymer network, and the boundary between mostly reacted and unreacted material where opposing transport pathways and the most chaotic and complex dynamics occur.

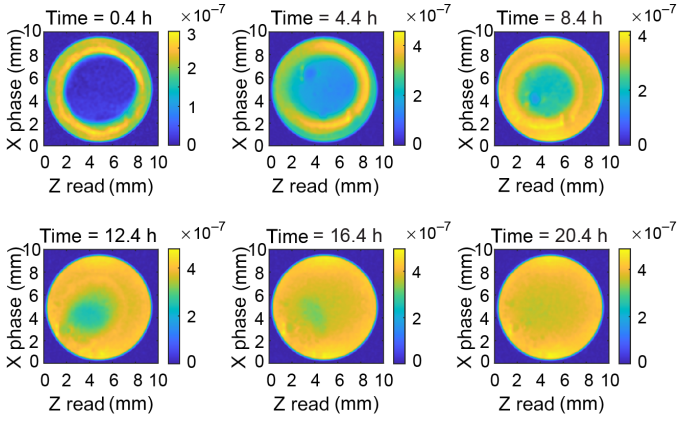

Fig. 2. MRI cross-sectional images of PDK acidolysis. Images of PDK-T403 in 5 M HCl are weighted by R_2, as described in Methods. The polymer was prepared with cylindrical initial geometry 8 mm in diameter and 6 mm in height, in a 10-mm NMR tube surrounded by approximately 1 ml of acid. Initially, there is only signal from the surrounding aqueous solution, and no signal from the PDK due to R_2 weighting. The axial images show that there is a reaction front that forms with high signal intensity on the outer rim of a PDK cylinder, clearly visible as a bright yellow ring surrounding the PDK which appears as a central blue disk. By $t = 20.4$ hours, the sample has fully deconstructed, and the final image has uniform intensity within the NMR tube.

behavior of the hydrolysis process, with swelling dominating the fastest early stage of the deconstruction and diffusion limiting the later stages of the reaction as it slows because of lack of randomization of the system (*22*, *23*).

Figure 2 depicts R_2-weighted MR images of PDK-T403 deconstruction in 5 M HCl. The axial images show that there is a reaction front that forms with high signal intensity on the outer rim of a PDK cylinder, clearly visible as a bright yellow ring surrounding the PDK that appears as a central blue disk. This reaction front, correlated with the swelling front of water moving into the polymer layers, represents the active area of hydrolytic bond cleavage and is present for the initial ~10 hours of the hydrolysis. After 10 to 12 hours, this swelling front has moved through the sample, and the remaining reaction is diffusion mediated. Figure S1 shows the initial PDK swelling ratio in three different acids over time: hydrochloric acid, hydrobromic acid, and sulfuric acid. Bromide, as the most chaotropic anion studied, leads to the fastest swelling behavior by aiding solubility, whereas the most kosmotropic anion, sulfate, leads to the slowest swelling behavior by hindering solubility. Changes in R_2 are largely attributed to the depolymerization reaction rather than the swelling process, as shown by a control experiment monitoring R_2 during polymer swelling (fig. S2 in the Supplementary Materials). Figures S3 and S4 in the Supplemental Materials demonstrate representative R_2 mapping to confirm R_2 localization and point-resolved ^{1}H spectroscopy obtained via reaction monitoring using deuterated acid, wherein signal is largely attributed to solvated polymer and liberated, protonated triamine monomer product. The change in magnetic resonance imaging (MRI)–derived surface areas shown in Fig. 2 can be used to calculate the instantaneous rate of change of the relative polymer cross-sectional area over time (figs. S5 and S6).

Analysis of these data requires examination of the physical and mathematical rate processes underlying the depolymerization process. For example, reaction and swelling behavior in unstirred vessels is marked by spatial separation of reactants and has been historically addressed with fractal-like kinetics (*22*). Hence, we turn to that methodology to further our analysis of the data in Fig. 2.

We note that nonlinear and nonuniform reaction rate laws are consistent with transport properties reported in fields beyond fractal mathematics, as is well recognized in the areas of heat transfer, mass transfer, and fluid mechanics. There is a rich history of work investigating transport and diffusion in polymer gels and networks (*24*–*26*). Power laws have also been used to study the problems of drug release from hydrogels and non-Newtonian fluid dynamics (*27*–*30*). The exponent in a power law describes a dimensional coordinate along a spatial or temporal axis and follows directly from a solution to differential equations of motion obeyed by the system (*31*, *32*). In the case of chemical kinetics, the molecularity of the reaction is the physical observable typically invoked to interpret the meaning of an exponent value. Although it is not universally described with fractal terminology, a noninteger exponent can follow logically when the effective surface area and dimensionality of a system evolve over the course of a reaction and points to a shift from anisotropic to isotropic diffusion of reactants. These notions have been lacking in the design of chemical recycling processes for plastic waste.

Fractal objects have long been known in mathematics through their key features of self-similarity and recursiveness upon iteration (*33*). Either generated theoretically or found randomly in nature, they capture patterns that are self-similar across extended length scales or relate parameters with nonlinear scaling through a relatively simple mathematic framework involving power laws with noninteger exponents. However, it was not until the 1960s that the term "fractal" appeared to provide a formalism for the fractional

dimensionality implied by noninteger exponents in power law scaling relations. This "fractal dimension" can conveniently parameterize rough topologies in space and time to precisely understand complex processes in real-world settings (*33*). Here, we describe the implementation of the fractal-based mathematics as they are below applied to rate law kinetics. The fractal dimension and Hurst exponent (*34*, *35*) are used to parameterize the time dependence of the reaction rate coefficient and molecularity.

In classical chemical kinetics, the rate constant k does not exhibit any time dependence, and the rate law and mechanism are consistent for the duration of the reaction. However, in diffusion-limited, heterogeneous systems, it has been observed that $k(t) \sim D(t)$, where D represents the self-diffusion coefficient, and the measured values of both coefficients may vary in time (*22*, *36*). In this case, $k(t) \propto t^{-h}$, and therefore, one may plot the instantaneous rate coefficient versus time as

$$\log k = -h \log t + \text{constant} \quad (1)$$

where $0 \leq h \leq 1$, and is the so-called Hurst exponent (*35*). In the classical limit, $h = 0$ because k is constant. Conversely, in diffusion-mediated reactions that are confined within non-Euclidean, fractal spaces, $h > 0$ and k is time variant. Furthermore, in systems with complex transport dynamics reflecting concurrent molecular and thermodynamic processes, h may also vary in time; this is termed "multifractal" behavior and indicates a changing fractal dimensionality (*37*–*39*).

In the three spatial dimensions of Euclidean geometry, it is immediately evident that the fractal dimension describes how surfaces or objects fill space, and nonlinear scaling between features such as surface area and volume may be conveniently expressed with a power law function (*40*). By extension, if we consider a temporal rather than spatial dimension, such as a time series, its fractal dimension will convey the jaggedness between time points (*41*). An idea of central importance is that the fractal dimension of a time series, and by extension the Hurst exponent, reports the degree to which a process is deterministic or random (*42*). The Hurst exponent relates to an autocorrelation function for a process in time with a power spectrum, $P(f)$, displaying exponential frequency dependence as

$$P(f) \propto f^{-\beta} \quad (2)$$

where f represents frequency and β is a scaling exponent (*43*, *44*). Notably, for Brownian motion, $\beta = 2$ and $h = (\beta - 1)/2 = 0.5$ (*45*, *46*). In general, lower values of h indicate higher fractal dimensionality or jaggedness in a time series. The so-called fractal dimension can be calculated as $n - h$ for an n-dimensional system. Multifractals involve more than one exponential parameter and as a result reflect the presence of multiple phenomena or processes taking place concurrently in a system. It should be noted that variation of h in time is evidence of multifractal behavior in the system.

For a bimolecular reaction to take place, two reactant molecules must collide. As they react, they become depleted and the reactant pairs decrease in time. Classically, it is assumed that the ensemble regains randomness (i.e., spatially distributed reactants) throughout the process. However, in the diffusion-limited case, it may become apparent that mixing cannot compensate for reactant pair depletion, and the topology of the reaction gains importance. A convenient way to parameterize this is with the order parameter, F, defined as

$$F = k_0 / k_{ss} \quad (3)$$

which is the ratio of the initial rate, k_0, to the steady-state value of k at long times, k_{ss}, achieved in low-dimensional systems, only after "self-ordering" is established. Self-ordering is understood as the spontaneous organization of an open, nonequilibrium system without external influence. In heterogeneous reactions, the reaction rate increases with the size of the reaction interface (*47*). In other words, the rate per unit surface area is constant. Upon inspection, it is also immediately evident that noninteger molecularity in the integrated rate law of a chemical reaction can be described by a fractal dimension or with the Hurst exponent. Thus, the rate coefficient can be plotted versus time on a log-log scale to reveal the Hurst exponent, h, as the slope. However, if the reaction rate coefficient k also changes nonlinearly in time, the time dependence of h can be revealed in turn by plotting the instantaneous rate of change of k. This is demonstrated in figs. S5 and S6, where imaging data as shown in Fig. 2 are presented as rates for PDK-T5000 decomposition in 5 M H_2SO_4.

Nonclassical behavior increases with diminishing cross-linking density

First, we investigated the effect of cross-linking density on the depolymerization kinetics. As shown in Fig. 3A, the polyetheramine cross-linker with lowest molar mass, T403, behaved classically with a rate coefficient that was constant in time. However, we found that for cross-linkers with increasing molar mass, which produces a PDK elastomer with lower cross-linking density, the fractal-like properties of the PDK hydrolysis reaction became more apparent (tables S1 and S2). These fractal properties emerged for unstirred reaction media via two-dimensional (2D) MRI, where the anisotropy of the PDK specimens—i.e., cylinders 8 mm in diameter and 6 mm in height, placed in a 10-mm NMR tube with acid—constrained the diffusion-limited, heterogeneous reaction in our observational window. Broadly, Fig. 3 demonstrates that decreasing the cross-linking density of the PDK network causes a reduction in the reaction rate. More specifically, Fig. 3A shows that cross-linker T403 with the lowest molar mass does not display fractal characteristics, as the rate coefficient is approximately constant in time; cross-linker T3000, with an intermediate molar mass, demonstrates a rate coefficient that linearly decreases in a manner adequately fitted by Eq. 1 in Fig. 3B. However, cross-linker T5000, with the highest molar mass, exhibits a rate coefficient that varies nonlinearly on the log–log scale in Fig. 3B, indicating multifractal behavior. It is remarkable that even in such a simple, self-similar system, these divergent behaviors become evident in the analysis of their deconstruction behaviors using MR methods.

With intermediate cross-linking density of PDK-T3000, initial experiments display a roughly bimodal distribution of rate coefficients that reflect a reaction that is fastest during the initial swelling phase and slows until hydrolysis completion. This is manifested as a discontinuity in a log-scale plot of NMR-derived PDK area versus time, shown in figs. S5 and S6, and appears with binary, quaternary, and ternary-level image thresholding.

Figure 4A shows the early- and late-stage rate coefficients (k_{early} and k_{late}, respectively) fit with classical first-order kinetics equations for the hydrolysis of PDK-T3000 in 5 M HCl. As the number of MRI thresholding levels increases from binary to quaternary, the fitted rate constant tends to decrease due to detection of finer detail in the MRI signal. Nonetheless, all three thresholding methods report the same trend of rate that decreases in time: In all cases, $k_{early} > k_{late}$.

To assess continuously changing rate coefficients, as well as to identify the Hurst exponent h, we test the temporal fractal reaction behavior by plotting the instantaneous rate coefficient, k, versus time on a logarithmic scale, as written in Eq. 1, and the results are shown in Fig. 4B. Here, the hydrolysis of PDK-T5000 in 5 M sulfuric acid data are shown in comparison to the swelling ratio. By plotting the instantaneous k, it is clear that the rate changes continuously even during the most rapid, swelling-mediated part of the reaction. By fitting k as a function of time on the log–log scale, it is possible to extract h as 0.74 ± 0.094.

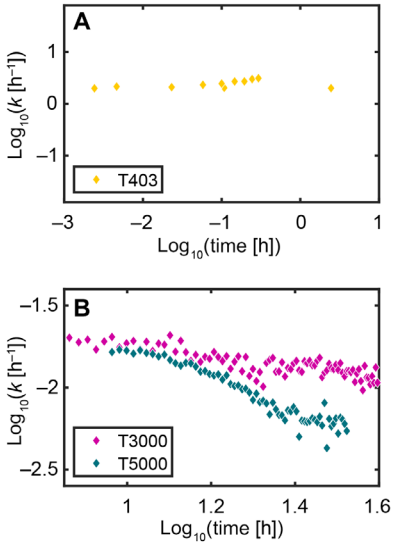

Fig. 3. Classical versus nonclassical rate behavior for different cross-linker sizes. Log–log plot of instantaneous k versus time for PDK hydrolysis in 5 M H_2SO_4 for PDK-T403, PDK-T3000, and PDK-T5000 after the initial swelling. (**A**) PDK-T403 (yellow) does not display fractal character as k remains classically time-independent; h~0 if fit to Eq. 1. (**B**) PDK-T3000 (magenta) displays nonclassical fractal character as $h = 0.32 \pm 0.032$ and fits well with Eq. 1. PDK-T5000 (blue) displays multifractal character as the decay in logarithmic k is nonlinear and cannot be fit with Eq. 1.

Table S1 in the Supplementary Materials shows the combinations of PDK molecular weight variant and acids that were tested, as well as the anticipated effect of the acid anion on the relative rate of hydrolysis. As illustrated in Fig. 1, kosmotropic (i.e., water ordering) ions that tend to order water also effectively slow the depolymerization process. The sulfate ion is the most kosmotropic anion of the series considered, and therefore leads to the lowest degree of polymer solvation, highest ordering of reactant species present, and slowest overall reaction.

Varying acid anion affects water–polymer interactions that mediate depolymerization

Next, we explore the effect of varying the acid anion on the depolymerization rate. By changing the solvation shell, this manipulates the effective surface area to which the reaction is initially constrained, thus leading to the multifractal behavior that is illustrated in Fig. 5. In general, multifractal behavior reflects numerous forces driving the system. Here, multifractal analysis can shed light on numerous complex features during PDK acidolysis, to the extent that some aspects of the process are characterized by cascades of scaling phenomena. These scaling phenomena affect the exponent in the power law and arise from physical means such as diffusion, convection, turbulence, et cetera. The same forces acting over an extended range of space- or timescales yield self-similar distributions, so we expect to observe fractal behavior. Multifractal behavior is evident if the Hurst exponent changes in time, as shown in Fig. 5B for PDK-T5000, calculated from the set of $k(t)$ reported in Fig. 5A. These changes are due to spatial inhomogeneity of reactant distribution between steps of the reaction, which hinders reactant pairing, leading to nonclassical behavior and variability between experiments that can manifest as lack of reproducibility. The sulfuric acid data appear to be time shifted because this acid, with the slowest kinetics, leads to swelling for longer times than HBr or HCl. Additional calculated h and F values for PDK hydrolysis are tabulated in table S2.

These results are relevant to concepts of molecular memory and fractional theories of Brownian motion, as discussed in (*48*). Fractional advection diffusion reaction models may provide valuable

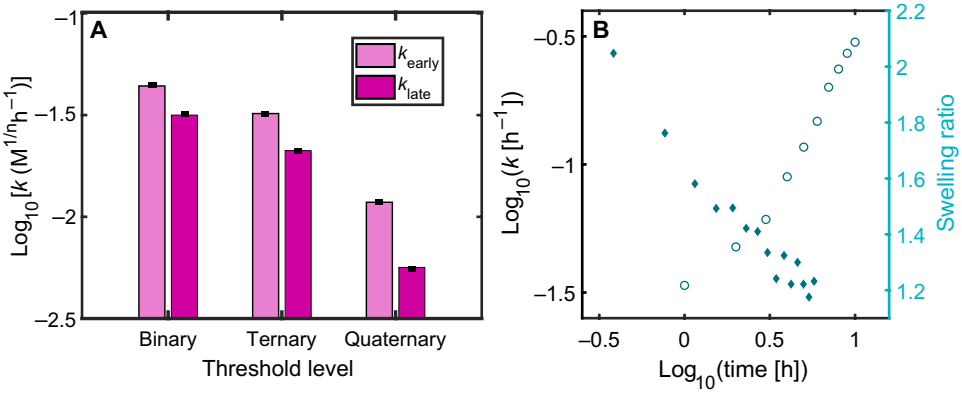

Fig. 4. Classical versus fractal kinetics analysis. (**A**) A comparison of classical fitting of PDK-T3000 in 5 M HCl rate constants with three levels of MRI thresholding for early (k_{early}) versus late (k_{late}) reaction with unconstrained reaction order. In all cases, the experimental fits demonstrate a consistent trend of decreasing rate as the reaction progresses in time. (**B**) A test of temporal fractal reaction rate behavior for the first 5 hours of hydrolysis of PDK-T5000 in 5 M H_2SO_4. PDK-T5000 has the lowest cross-linking density of the materials tested. The left ordinate reports the log of instantaneous k (blue diamonds), compared to the normalized volumetric swelling ratio on the right ordinate (blue circles). These 5 hours are the fastest of the overall reaction, as rate is an extensive property dependent on effective surface area. Fitting $k(t)$ according to Eq. 1 yields $h = 0.74 \pm 0.094$.

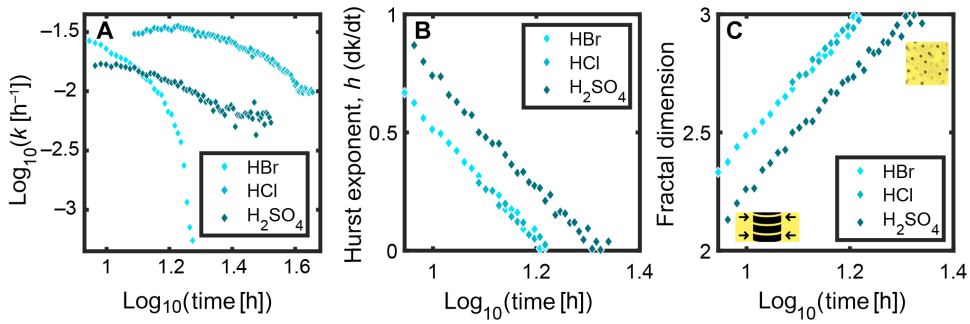

Fig. 5. Fractal analysis of nonlinear acidolysis kinetics. (**A**) The instantaneous rate coefficient, *k*, versus time for PDK-T5000 deconstructing in 5 M HBr (light blue), HCl (medium blue), and H_2SO_4 (dark blue) acid solutions after the initial swelling phase. Data were plotted according to Eq. 1 in the text. (**B**) The PDK-T5000 Hurst exponent and (**C**) fractal dimension change with time according to MRI data and Eq. 1. The sulfuric acid data appear to be time shifted because this acid, with the slowest kinetics, leads to swelling for longer times than HBr or HCl and gives rise to the largest solvation shell. The graphics in (C) aid interpretation of the changing fractal dimension, indicating evolution from roughly 2D, anisotropic initial topography and dynamics toward 3D, isotropic topography and dynamics upon completion.

methods for anchoring these experimental results in theory; however, their implementation is not necessarily straightforward in the context of evolving fractal pore networks and surface catalysis. This topic is considered in greater detail in the Discussion.

Increasing fractal dimension reveals diminishing configurational anisotropy

Water diffusion in the initial swelling front appears to be 1D with radial symmetry around the PDK surface for the initial stage of reaction, as demonstrated in Fig. 2. As hydrolysis begins to occur while swelling moves radially inward, the roughness of the polymer surface increases, leading to a corresponding increase in the effective dimensionality and surface area for hydrolysis as shown in Fig. 5B. This can provide a physical interpretation of a noninteger exponent in the rate law. Moreover, this observation is consistent with a system whose effective surface area and dimensionality evolve over the course of a reaction and points to a shift from anisotropic to isotropic diffusion of reactants.

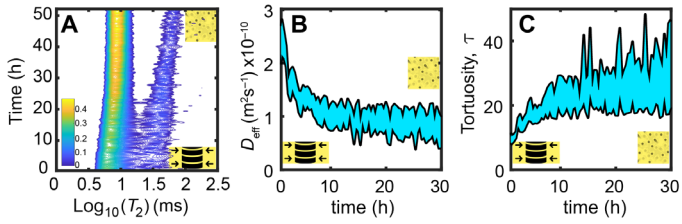

Fig. 6. In situ NMR relaxometry and diffusometry of PDK acidolysis. (**A**) Time-resolved measurement of T_2 during the hydrolysis of PDK-T5000 in 5 M H_2SO_4. Laplace inversion was accomplished with the Lawson and Hanson algorithm in the Prospa software; the color bar indicates amplitude of the contour plot on an arbitrary scale. Time-resolved measurement of D_{eff} and τ during the hydrolysis of PDK-T5000 in 5 M HBr in (**B**) and (**C**), respectively. D_{eff} was fit with a monoexponential to reflect the average, bulk diffusion of the triketone monomer and water in solution together; the shaded region of the plot reflects error. The graphics connect relaxometry, diffusometry, and tortuosity to the analysis of changing fractal dimension in Fig. 5C.

Relaxometry and self-diffusion unravel macroscopic molecular dynamics

This shift toward isotropic molecular motion as the PDK system evolves from polymer, to mixed chain-length oligomers, then to monomers in aqueous solution is reflected in the time-resolved measurement of spin-spin relaxation, where $T_2 = R_2^{-1}$, and *D*, the self-diffusion coefficient as determined by Carr–Purcell–Meiboom–Gill (CPMG) and pulsed gradient spin echo (PGSE) experiments, respectively. From the self-diffusion coefficient, the tortuosity (τ) can be calculated as

$$\tau(t) = D_{H_2O} / D_{eff}(t) \quad (4)$$

as described in (*49*), where $D_{eff}(t)$ is the effective, time-dependent self-diffusion coefficient. Tortuosity can thus be understood as the ratio of free to restricted diffusion within a system and is immediately related to the entanglement of a polymer network. Values for $T_2(t)$, $D_{eff}(t)$, and τ(t) are presented in Fig. 6 for PDK-T5000 deconstructing in H_2SO_4 and HBr, respectively. The shortening of R_2 throughout the hydrolysis and sharpening into two distinct environments reflects increasing molecular mobility as the monomer product is produced in Fig. 6A. The initial broad distribution of R_2 values represents polymer swelling when the system is maximally heterogeneous in terms of macroscopic phases.

Likewise, the decrease in bulk diffusivity and corresponding increase in tortuosity after 2 hours reflects incorporation of the triketone monomer unit into the measured aqueous environment, as illustrated in Fig. 6 (B and C). The initial value of D_{eff} (for $t <$ 2 hours) measured in the PGSE experiment primarily reflects the bulk diffusion of water, when the molecular tumbling is the most unhindered and least tortuous. As the monomer concentration increases in solution, flow paths become more irregular, and tortuosity increases as diffusivity drops. After the saturation point has been reached, D_{eff} and τ reach a steady state; additional insoluble product precipitates and settles to the base of the reaction vessel.

Here, we note that the fractal model provides parameters that better describe the acidolysis process than "*k*"—T_2 and *D* measurements do not adequately describe the reaction kinetics and are primarily provided to aid with interpretation of the qualitative physical meaning of the fractal model parameters. In the industrial setting where the progress or completeness of a depolymerization reaction is important for efficient materials recovery, it is desirable to identify

a metric that offers 1:1 correspondence with the reaction progress and changes monotonically between start and end points. This is something that the parameters from the fractal analytical model (h and F) provide and are further desirable because they do not require observation of the entire reaction to be measured. To measure h, one must only record the instantaneous rate of the reaction between two successive time points. To measure F, one must record only the initial and final (equilibrium) rates.

Our measured values of T_2 and D are somewhat variable (because of internal gradients in magnetic field, temperature, B_0 or radio frequency (rf) field inhomogeneity, experimental parameters, the part of the spectral density that is sampled, among other things) and therefore are poor descriptors of the process because there lacks a 1:1 correlation between the absolute value obtained from different instruments and the reaction progress. Thus, to draw direct comparisons of the depolymerization in differing media by plotting a "single number" from each experiment over time, T_2 and D are poor choices because their shifts between resolved values and broad distributions—reflecting heterogeneity, among other things—makes developing ubiquitous analysis strategies challenging and motivates the implementation of alternative parameters such as h and F proposed here.

DISCUSSION

It is critical to develop experimental and analytical methods to characterize polymer deconstruction with chemical, spatial, and temporal resolution. The limitations of classical kinetics fitting approaches are well documented (*50*) and are immediately apparent when the reaction order and the molecularity are unconstrained and vary throughout heterogeneous reactions. Moreover, other commonly measured NMR parameters, such as T_2 and D, fail to adequately capture the complexities of evolving polymer systems.

Fractals and multifractals are useful mathematical tools for disentangling complex scaling relations in data because one can approximate both the spatial topology of a polymer as well as the temporal behavior of a heterogeneous chemical reaction. The principal goal of this work is to present strategies to report, then treat, the nonlinearity in the process of tuning acidolysis reactions by variation of parameters such as the molecular weight of monomer units and the choice of acid anion. In the present PDK acidolysis study, we find that the hydrolysis rate coefficient decreases with time. The fitted reaction order also tends to be noninteger and decreases with time. A key correlation revealed by our analyses is that polymer deconstruction reactions constrained to irregular surfaces may occur at rates described by fractals evolving in time.

This approach can be used with any instantaneously calculated reaction rate coefficient, k. Here, k was derived from the changing relative reactant area from MR images, but the fractal analysis method for evaluating reaction kinetics can also be applied to 1D or 2D NMR spectra, microscopy, or intensity data from any other spectroscopy (such as ultraviolet-visible, infrared, etc.) in which the intensity changes of a given resonance is indicative of a reaction process. Therefore, we propose that this could be a widely useful method that is not limited to imaging data.

We note that MRI and relaxometry provide convenient ways of localizing and detecting a reaction front, respectively, if an appropriate contrast parameter can be identified for a given system and if this information is valuable in a given context. These findings are tempered by the recognition that the broader utility of an MRI-based kinetics analysis is limited to the scope of comparisons between MRI instruments. Image thresholding is sensitive to fluctuations in relative signal intensity, which may limit the comparative robustness of this analysis with, for example, high Q MRI probes that are susceptible to detuning as the ionic concentration of the strong acid changes. Moreover, it is possible to incorrectly attribute phenomena arising from different regions of a spatially heterogeneous sample as homogeneously nonlinear behavior. Thus, care must be taken with the interpretation of these results, and the continued development of experiments that provide resolution of spatially and temporally inhomogeneous observables is warranted. It is beneficial to compare results with independently performed relaxometry, diffusion, and reaction monitoring experiments from other instruments to gain a broad understanding of the process of polymer deconstruction as a whole. We have attempted to do so herein.

Comparison of experimental data with numerical simulations can further guide this process. Polymers are known to be fractal objects with self-similarity in length scales ranging from the size of the monomer(s) to the total chain length (*33*, *38*, *51*). However, by definition (*34*, *37*, *39*), fractal objects may be categorized as random or nonrandom spatial or temporal patterns. While this very fact suggests that there may exist a mathematical relationship linking spatial and temporal objects, this work only attempts to demonstrate the fractal characteristics of the temporal process of depolymerization kinetics. On the basis of literature knowledge of polymers as archetypal fractals, we reveal a connection between objects exhibiting spatial fractal structures while presenting dynamic processes with fractal kinetics in time—an intriguing link between structure and dynamics.

Molecular self-diffusion is a central phenomenon behind this correlation, both of water in restricted environments and of the polymer chains themselves. To rigorously prove this connection between spatial and temporal fractal-like behavior, we posit that the reaction-diffusion equation must be solved for the relevant system with time-dependent, non-Euclidean boundary conditions. An exemplary modified reaction-diffusion equation may be given by the O'Shaugnessy and Procaccia (OP) model (*52*, *53*), but the time-dependent boundary conditions are nontrivial to describe and implement. These topics are the subject of current and crucial works. Broadly, though, we shall provide a holistic sketch of the results that consideration of this equation might yield. Spherical Bessel functions are solutions for the cylindrically symmetric geometries we have considered here, assuming that the boundary conditions are Euclidean (*54*). However, these solutions are modified by the restriction of fractal pore boundaries that are not monodisperse (*48*, *55*–*58*) and must therefore be integrated over in the range present in the heterogeneous pore network. Moreover, because the pore network is also deconstructing in time, the time-dependent amplitudes of pore sizes must be weighted accordingly.

It is important to note that within suitably restricting pore networks, the motion of water is non-Brownian, which manifests as a velocity autocorrelation function with a long-time tail (*59*), although the deconstruction of the polymer network serves to remove restriction and permit additional free, Brownian modes of aqueous self-diffusion. It is also nontrivial to assign the time-dependent amplitudes for the linear combination of these distinct modes of aqueous diffusion that exist in superposition with each other for the entirety of the observational window.

If the various D values were known, it may be possible to solve the OP model for $k(t)$ and extract $h(t)$; however, there is yet another foreseeable complication. The system we consider has diffusive components for water, polymer, and deconstructed polymer fragments. These components may not necessarily be resolved from each other. For example, free water is subject to simple Brownian diffusion, as discussed above, and represents the highest frequency moiety; correlated (and hence slower) restricted diffusion of water may not be spectrally resolved from the free diffusion of released monomers. Consideration of polymer and oligomer diffusion, which may be treated with reptation, Rouse, and Zimm models of polymer dynamics (*51*), describes the low-frequency modes of diffusion that are difficult to disentangle from each other experimentally. Nonetheless, it is essential to discern the accurate range and assignment of D values for the system of reaction–diffusion equations for numerical simulations to validate the fractal kinetics model presented here.

In addition, automation of image thresholding and segmentation is a key step in the analytical workflow that upcoming work must address to increase robustness, as the parameters in the resulting rate power law are highly sensitive to small changes in the segmented image intensity. Thus, we recommend that improvements in image segmentation algorithms be considered for future implementation.

A grand challenge of the present global economy is to transition from a linear flow of materials, which depletes and squanders resources, to sustainable processes that leverage resource circularity. This paradigm shift will rely on widespread implementation of chemically recyclable plastics with high materials efficiency and low process intensity. To adopt these materials on the industrial scale, it is necessary to first understand the phenomena that influence their recycling properties, and then to develop robust metrics that succinctly describe these phenomena and properties. To this end, we report a fractal method for tracking polymer recycling that adequately captures deconstruction nonlinearity, yet directly yields straightforward numeral parameters for immediate analysis. These capabilities provide much needed tools to enable and perfect chemical recycling processes for mechanically processed plastic waste that are heterogeneous throughout their deconstruction in materials recovery facilities.

MATERIALS AND METHODS

Experimental design

The principal objective of this study was to monitor the PDK depolymerization process depicted in Fig. 1 and to track the macroscopic reaction kinetics through MRI, relaxometry, and diffusometry. PDK elastomers were synthesized by ball-milling a triketone monomer (1,10-*bis*(2-hydroxy-4,4-dimethyl-6oxocyclohex-1-en-1-yl)decane-1,10-dione) (*8*) with tribranched amine-terminated polypropylene glycol cross-linkers T403, T3000, and T5000 (Huntsman), whose molar masses are nominally 403, 3000, and 5000 g mol^{-1}, respectively. A detailed description is provided in the "PDK synthesis" section of the Supplementary Materials. Acids were prepared in 5 M concentration of HBr, HCl, and H_2SO_4. These chemicals were obtained from Sigma-Aldrich and used as received.

NMR relaxometry measurements were performed at room temperature with an NMR-MOUSE (Mobile Universal Surface Explorer) PM25 0.3 T unilateral magnet (*13*, *60*) and a Magritek Kea II spectrometer at a ^{1}H resonant frequency of 13.11 MHz. A CPMG pulse sequence (*61*, *62*) was used to detect R_2 relaxation and fit with a Laplace inversion algorithm in Prospa v3.61 software from Magritek (Malvern, PA). For all experiments, $\pi/2$ rf pulse lengths were 2.5 μs, the delay between π rf pulses was 55 μs, 1500 spin echoes were obtained for CPMG detection, and the repetition time for signal averaging was 2.4 s to sum 128 CPMG transient signals. To cancel artifacts arising from pulse imperfections, the initial $\pi/2$ rf pulse and the receiver were cycled between +x and −x phase while holding the π rf pulse phase constant at +y. Laplace inversion was accomplished with the Lawson and Hanson algorithm in the Prospa software, with a smoothing value of 0.9 chosen by minimizing χ^2 without oversmoothing.

Imaging and PGSE experiments were carried out with a Pure Devices 0.55 T Magspec magnet interfaced to Drive-L RF-100 and Gradient-600 amplifiers and an actively damped Q probe (Pure Devices GmbH, Germany), at a ^{1}H resonant frequency of 24.36 MHz, and temperature controlled at 29°C. Images were acquired using a standard spin echo pulse sequence with an echo time of 5 ms and a repetition time of $5T_1 = 1$ s for the 5 M strong acids, to maximize signal from the aqueous acid and minimize signal from solid PDK with R_2 weighting. This was achieved in the standard gradient spin echo sequence by making the echo time long enough such that signal intensity only arose from the long R_2 component (*20*). When the echo time is long relative to the fast R_2 parts of the sample, only aqueous parts with slow R_2 relaxation will retain sufficient phase coherence in the delay before the refocusing pulse. This was invoked to create "blank space images" in which bright parts correspond to bulk water and dark parts correspond to polymer. After thresholding, inverting the brightness ordering of the bins creates an effective image of the polymer. A 10-mm square field of view was chosen, corresponding to a 64 × 64 sampling grid with a slice thickness of 5 mm for axial images centered on polymer cylinders 6 mm in height and 8 mm in diameter placed in approximately 1 cm^3 of acid. Zero-filling interpolated the square pixel resolution from 156.2 to 39.1 μm (*20*) The PGSE experiments were carried out with a 10-ms echo time, 2.5-s repetition time, with the diffusion-encoding b-value ramped from 2×10^9 to 10×10^9 s m^{-2} to maximize sensitivity to aqueous diffusion while minimizing detection of the slower modes of polymer diffusion.

Localized spectroscopy and R_2-mapping experiments were performed with a 9.4-T Bruker Avance Neo spectrometer equipped with a Micro 5 microimaging probe, at a ^{1}H resonant frequency of 400 MHz, using ParaVision 360 v3.2 software. Temperature was held constant at 20°C. Multislice, multiecho (MSME) experiments were conducted for R_2-mapping, and point-resolved spectroscopy experiments provided localized ^{1}H spectra. Voxel sizes were 1 × 2 × 2 mm (X-Y-Z), with 32,768 points collected during acquisition times of 262 ms, with a bandwidth of 125 kHz, a dwell time of 4 μs for spectral resolution of 1.91 Hz per point, 10-s repetition time, 15-ms echo time, and 128 scans for signal averaging corresponding to 20-min experiments. Square images were acquired with 256 × 256 points within a 10-mm by 10-mm field of view, and eight slices with a slice thickness of 1 mm. For MSME experiments, the echo time was varied from 4 to 64 ms in 16 steps incremented by 4 ms, and repetition time was decreased to 1.5 s to maintain a total experiment time of 20 min.

Statistical analysis

Data analysis and fitting were completed in MATLAB (MathWorks, Natick, MA). The workflow for kinetics analysis of imaging data involves (i) load the raw image data and stack it in a 3D array (two

dimensions are spatial; the third dimension is time); (ii) convert the 3D image array to a segmented 3D array with an inverted intensity scale (thresholding methods are binary, with bins = 0, 1; ternary, with bins = 1, 2, 3; and quaternary, with bins = 1, 2, 3, 4); (iii) sum the area in each 2D image; collapse to a vector of area as a function of time, and rescale so the initial point matches for all three methods (binary ➔ 1; ternary ➔2 + 3; quaternary ➔2, 3, 4); (iv) calculate the instantaneous rate as the derivative between points; and (v) plot the log of k versus the log of time. A linear fit indicates a consistent fractal dimension, and h is extracted by fitting the slope. If the time variation of k is nonlinear, then the derivative $^{\partial k}/_{\partial t}$ can be calculated to plot both h and the fractal dimension over time. The fractal dimension is calculated as $3 - h$ for a 3D system, or $2 - h$ for a 2D system.

It is noted that binary thresholding does not provide sufficient detail for fine signal changes, leading to steep drop-offs and sudden jumps in the calculated relative PDK area over time. On the other hand, quaternary (four-level) thresholding is highly sensitive to noise and other small variations in signal intensity as the reaction proceeds and the relative signal increases from the deconstructing and swelling polymer. Therefore, ternary (three-level) thresholding is chosen for automated image segmentation in the majority of this work. The Otsu algorithm is used here for automated choice of threshold levels (*63*).

Binary thresholding converts the image into zeroes and ones based on a single threshold value for signal intensity. Ternary thresholding uses the standard MATLAB implementation of the Otsu algorithm to select two threshold levels by minimizing variance within the bins and maximizing variance between the bins. This is accomplished through a weighted sum of variances of the two classes: The weights are iteratively varied as a function of the threshold level until the optimal threshold is identified. Therefore, the bins may not be chosen in exactly equidistant steps. This widely accepted method is essentially a discrete analog of Fisher's discriminant analysis (*64*) and results in an image converted to values of ones, twos, and threes. This allows ready identification of water, polymer, and the bright "reaction front" as zones ascribed to a given number on the basis of their ordering of brightness, directly enabling area calculations by summing the relevant number(s). Quaternary thresholding was implemented in the same manner, but with four bins rather than three, resulting in an image of ones, twos, threes, and fours.

Supplementary Materials

This PDF file includes:
Supplementary Text
Figs. S1 to S6
Tables S1 and S2
Legends for Movies S1 to S18
Legends for Software S1 and S2

Other Supplementary Material for this manuscript includes the following:
Movies S1 to S18
Software S1 and S2

REFERENCES AND NOTES

1. World Economic Forum, Ellen MacArthur Foundation and McKinsey & Company, "The New Plastics Economy: Rethinking the future of plastics" (World Economic Forum, 2016).
2. United Nations Environment Programme, Ellen MacArthur Foundation, "The Global Commitment 2020 Progress Report" (United Nations Environment Programme, 2019).
3. Ellen MacArthur Foundation, "The New Plastics Economy: Catalysing action" (2017).
4. A. Rahimi, J. M. García, Chemical recycling of waste plastics for new materials production. *Nat. Rev. Chem.* **1**, 0046 (2017).
5. M. H. Levitt, *Spin Dynamics: Basics of Nuclear Magnetic Resonance* (Wiley, ed. 2, 2008).
6. A. Abragam, *The Principles of Nuclear Magnetism* (Clarendon Press, 1983).
7. C. Slichter, *Principles of Magnetic Resonance* (Springer, ed. 3, 1990).
8. P. R. Christensen, A. M. Scheuermann, K. E. Loeffler, B. A. Helms, Closed-loop recycling of plastics enabled by dynamic covalent diketoenamine bonds. *Nat. Chem.* **11**, 442–448 (2019).
9. J. Demarteau, A. R. Epstein, P. R. Christensen, M. Abubekerov, H. Wang, S. J. Teat, T. J. Seguin, C. W. Chan, C. D. Scown, T. P. Russell, J. D. Keasling, K. A. Persson, B. A. Helms, Circularity in mixed-plastic chemical recycling enabled by variable rates of polydiketoenamine hydrolysis. *Sci. Adv.* **8**, eabp8823 (2022).
10. B. A. Helms, Polydiketoenamines for a circular plastics economy. *Acc. Chem. Res.* **55**, 2753–2765 (2022).
11. A. R. Epstein, J. Demarteau, B. A. Helms, K. A. Persson, Variable amine spacing determines depolymerization rate in polydiketoenamines. *J. Am. Chem. Soc.* **145**, 8082–8089 (2023).
12. B. Blümich, J. Perlo, F. Casanova, Mobile single-sided NMR. *Prog. Nucl. Magn. Reson. Spectrosc.* **52**, 197–269 (2008).
13. G. Eidmann, R. Savelsberg, P. Blümler, B. Blümich, The NMR MOUSE, a mobile universal surface explorer. *J. Magn. Reson. A* **122**, 104–109 (1996).
14. J. Perlo, F. Casanova, B. Blümich, Profiles with microscopic resolution by single-sided NMR. *J. Magn. Reson.* **176**, 64–70 (2005).
15. E. Fukushima, S. B. W. Roeder, *Experimental Pulse NMR* (CRC Press, 2018).
16. K. Saalwächter, Proton multiple-quantum NMR for the study of chain dynamics and structural constraints in polymeric soft materials. *Prog. Nucl. Magn. Reson. Spectrosc.* **51**, 1–35 (2007).
17. K. Saalwächter, P. Ziegler, O. Spyckerelle, B. Haidar, A. Vidal, J.-U. Sommer, ^{1}H multiple-quantum nuclear magnetic resonance investigations of molecular order distributions in poly(dimethylsiloxane) networks: Evidence for a linear mixing law in bimodal systems. *J. Chem. Phys.* **119**, 3468–3482 (2003).
18. A. Papon, K. Saalwächter, K. Schäler, L. Guy, F. Lequeux, H. Montes, Low-field NMR investigations of nanocomposites: Polymer dynamics and network effects. *Macromolecules* **44**, 913–922 (2011).
19. K. Saalwächter, W. Chassé, J.-U. Sommer, Structure and swelling of polymer networks: Insights from NMR. *Soft Matter* **9**, 6587 (2013).
20. B. Blümich, *NMR Imaging of Materials* (Clarendon Press, 2003).
21. M. J. McCarthy, J. R. Heil, Measurement of acid diffusion in canned vegetables using pH sensitive indicators. *J. Food Sci.* **53**, 494–495 (1988).
22. R. Kopelman, Fractal reaction kinetics. *Science* **241**, 1620–1626 (1988).
23. D. Mohanta, Solvent effect on equilibrium organization of confined polymers. *Soft Matter* **19**, 4991–5000 (2023).
24. S. P. O. Danielsen, H. K. Beech, S. Wang, B. M. El-Zaatari, X. Wang, L. Sapir, T. Ouchi, Z. Wang, P. N. Johnson, Y. Hu, D. J. Lundberg, G. Stoychev, S. L. Craig, J. A. Johnson, J. A. Kalow, B. D. Olsen, M. Rubinstein, Molecular characterization of polymer networks. *Chem. Rev.* **121**, 5042–5092 (2021).
25. R. Wang, M. K. Sing, R. K. Avery, B. S. Souza, M. Kim, B. D. Olsen, Classical challenges in the physical chemistry of polymer networks and the design of new materials. *Acc. Chem. Res.* **49**, 2786–2795 (2016).
26. A. Kusoglu, T. J. Dursch, A. Z. Weber, Nanostructure/swelling relationships of bulk and thin-film PFSA ionomers. *Adv. Funct. Mater.* **26**, 4961–4975 (2016).
27. P. I. Lee, Kinetics of drug release from hydrogel matrices. *J. Control. Release* **2**, 277–288 (1985).
28. M. Javidi Sarafan, R. Alizadeh, A. Fattahi, M. Valizadeh Ardalan, N. Karimi, Heat and mass transfer and thermodynamic analysis of power-law fluid flow in a porous microchannel. *J. Therm. Anal. Calorim.* **141**, 2145–2164 (2020).
29. R. Cheng, F. Meng, C. Deng, H.-A. Klok, Z. Zhong, Dual and multi-stimuli responsive polymeric nanoparticles for programmed site-specific drug delivery. *Biomaterials* **34**, 3647–3657 (2013).
30. A. Rösler, G. W. M. Vandermeulen, H.-A. Klok, Advanced drug delivery devices via self-assembly of amphiphilic block copolymers. *Adv. Drug Deliv. Rev.* **64**, 270–279 (2012).
31. J. Welty, G. Rorrer, D. Foster, *Fundamentals of Momentum, Heat, and Mass Transfer* (Wiley, ed. 6, 2014).
32. A. Nachman, S. Taliaferro, Mass transfer into boundary layers for power law fluids. *Proc. R. Soc. Lond. Ser. A* **365**, 313–326 (1979).
33. B. Mandelbrot, How long is the coast of Britain? Statistical self-similarity and fractional dimension. *Science* **156**, 636–638 (1967).
34. B. B. Mandelbrot, Self-affine fractals and fractal dimension. *Phys Scr* **32**, 257–260 (1985).
35. H. E. Hurst, Long-term storage capacity of reservoirs. *Trans. Am. Soc. Civil Eng.* **116**, 770–799 (1951).

36. M. Smoluchowski, Versuch einer mathematischen Theorie der Koagulationskinetik kolloider Lösungen. *Z. fur Phys. Chem.* **92U**, 129–168 (1918).
37. M. Frame, A. Urry, *Fractal Worlds* (Yale Univ. Press, 2019).
38. A. Bunde, S. Havlin, Eds. in *Fractals and Disordered Systems* (Springer Berlin Heidelberg, 1996).
39. K. Falconer, *Fractal Geometry* (John Wiley & Sons, Ltd, 2003).
40. S. Qiu, M. Yang, P. Xu, B. Rao, A new fractal model for porous media based on low-field nuclear magnetic resonance. *J. Hydrol.* **586**, 124890 (2020).
41. M. Kale, F. Butar Butar, Fractal analysis of time series and distribution properties of Hurst exponent. *J. Math. Sci. Math. Educ.* **5**, 8–19 (2011).
42. E. E. Peters, *Chaos and Order in the Capital Markets: A New View of Cycles, Prices, and Market Volatility* (John Wiley & Sons Inc., ed. 2, 1996).
43. A. Schaefer, J. S. Brach, S. Perera, E. Sejdić, A comparative analysis of spectral exponent estimation techniques for $1/f^{\beta}$ processes with applications to the analysis of stride interval time series. *J. Neurosci. Methods* **222**, 118–130 (2014).
44. A. Eke, P. Herman, L. Kocsis, L. R. Kozak, Fractal characterization of complexity in temporal physiological signals. *Physiol. Meas.* **23**, R1–R38 (2002).
45. B. B. Mandelbrot, J. W. Van Ness, Fractional Brownian Motions, Fractional Noises and Applications. *SIAM Rev.* **10**, 422–437 (1968).
46. J. Geweke, S. Porter-Hudak, The estimation and application of long memory time series models. *J. Time Ser. Anal.* **4**, 221–238 (1983).
47. C. F. Wenzel, *Lehre Von Der Verwandtschaft Der Korper* (Kessinger Publishing, 1777).
48. J. Ślęzak, R. Metzler, Minimal model of diffusion with time changing Hurst exponent. *J. Phys. A Math Theor.* **56**, 35LT01 (2023).
49. M. P. Hollewand, L. F. Gladden, Transport heterogeneity in porous pellets—I. PGSE NMR studies. *Chem. Eng. Sci.* **50**, 309–326 (1995).
50. J. Tóth, A. L. Nagy, D. Papp, *Reaction Kinetics: Exercises, Programs and Theorems* (Springer New York, 2018).
51. M. Doi, S. F. Edwards, *The Theory of Polymer Dynamics* (the Clarendon Press, Oxford Univ. Press, 1986).
52. B. O'Shaughnessy, I. Procaccia, Analytical solutions for diffusion on fractal objects. *Phys. Rev. Lett.* **54**, 455–458 (1985).
53. S. Wang, Z. Ma, H. Yao, Fractal diffusion model used for diffusion in porous material within limited volume of stiff container. *Chem. Eng. Sci.* **64**, 1318–1325 (2009).
54. J. Crank, *The Mathematics of Diffusion* (Oxford Univ. Press, ed. 1, 1979).
55. M. Giona, First-order reaction–diffusion kinetics in complex fractal media. *Chem. Eng. Sci.* **47**, 1503–1515 (1992).
56. M.-O. Coppens, G. F. Froment, Diffusion and reaction in a fractal catalyst pore—I. Geometrical aspects. *Chem. Eng. Sci.* **50**, 1013–1026 (1995).
57. C. McGreavy, J. S. Andrade, K. Rajagopal, Consistent evaluation of effective diffusion and reaction in pore networks. *Chem. Eng. Sci.* **47**, 2751–2756 (1992).
58. D. Bolster, D. A. Benson, M. M. Meerschaert, B. Baeumer, Mixing-driven equilibrium reactions in multidimensional fractional advection–dispersion systems. *Physica A* **392**, 2513–2525 (2013).
59. J. Stepišnik, P. T. Callaghan, The long time tail of molecular velocity correlation in a confined fluid: Observation by modulated gradient spin-echo NMR. *Phys. B Condens. Mater.* **292**, 296–301 (2000).
60. B. Blümich, J. Anders, When the MOUSE leaves the house. *Magn. Reson* **2**, 149–160 (2021).
61. H. Y. Carr, E. M. Purcell, Effects of diffusion on free precession in nuclear magnetic resonance experiments. *Phys. Rev.* **94**, 630–638 (1954).
62. S. Meiboom, D. Gill, Modified spin-echo method for measuring nuclear relaxation times. *Rev. Sci. Instrum.* **29**, 688–691 (1958).
63. N. Otsu, A threshold selection method from gray-level histograms. *IEEE Trans. Syst. Man Cybern.* **9**, 62–66 (1979).
64. R. A. Fisher, The use of multiple measurements in taxonomic problems. *Ann. Eugen.* **7**, 179–188 (1936).

Acknowledgments: We acknowledge insightful conversations with B. Blümich, M. McCarthy, K. McCarthy, and M. Augustine. We thank H. Celik, R. Giovine, and UC Berkeley's NMR facility in the College of Chemistry (CoC-NMR) for spectroscopic assistance. The CoC-NMR instrument used in this work is supported by the National Science Foundation under grant no. 2018784. **Funding:** This work was funded by the U.S. Department of Energy (DOE), Office of Science, Office of Basic Energy Sciences, Materials Sciences and Engineering Division under contract no. DE-AC02-05-CH11231 Unlocking Chemical Circularity in Recycling by Controlling Polymer Reactivity Across Scales program CUP-LBL-Helms. Work at the Molecular Foundry—including PDK synthesis, characterization, and acidolysis—was supported by the Office of Science, Office of Basic Energy Sciences, of the U.S. Department of Energy under contract no. DE-AC02-05CH11231. **Author contributions:** The CRediT author contributions are as follows: Conceptualization: S.N.F., J.A.R., B.A.H., and M.H. Methodology: S.N.F. and J.A.R. Investigation: S.N.F., M.H., and M.S. Visualization: S.N.F., S.H., and M.H. Supervision: J.A.R. and B.A.H. Writing—original draft: S.N.F. Writing—review and editing: S.N.F., S.H., J.A.R., and B.A.H. **Competing interests:** The authors declare the following competing interests: B.A.H. is an inventor on the U.S. provisional patent application 62/587,148 submitted by Lawrence Berkeley National Laboratory that covers PDKs, as well as aspects of their use and recovery. B.A.H. and M.H. are inventors on the US provisional patent application 63/390,962 submitted by Lawrence Berkeley National Laboratory that covers biorenewable PDKs, as well as aspects of their use and recovery. B.A.H. has a financial interest in Cyklos Materials and Sepion Technologies. The remaining authors declare that they have no competing interests. **Data and materials availability:** Processed data and codes used in the analyses are available in the Supplementary Materials. All raw MRI and NMR data are available from Dryad (https://doi.org/10.5061/dryad.k0p2ngfdw). The PDK materials used in this study can be provided by B.A.H. pending scientific review and a completed material transfer agreement. Requests for the PDK materials should be submitted to: foundry.lbl.gov. All data needed to evaluate the conclusions in the paper are present in the paper and/or the Supplementary Materials.

Submitted 11 October 2023
Accepted 28 February 2024
Published 3 April 2024
10.1126/sciadv.adl0568